Available online at www.sciencedirect.com
SCIENCE DIRECT®

Earth and Planetary Science Letters 214 (2003) 1–9

EPSL

www.elsevier.com/locate/epsl

On the support of the Tharsis Rise on Mars

Shijie Zhong [a,*], James H. Roberts [b]

[a] Department of Physics, University of Colorado at Boulder, Boulder, CO 80309, USA
[b] Department of Astrophysical and Planetary Sciences, University of Colorado at Boulder, Boulder, CO 80309, USA

Received 25 February 2003; received in revised form 10 June 2003; accepted 7 July 2003

Abstract

The most significant long-wavelength geoid and topographic anomalies on Mars are associated with the Tharsis Rise [Smith et al., Science 286 (1999) 94–97; Smith et al., Science 284 (1999) 1495–1503]. However, the origin of the elevated geoid and topography in the Tharsis region remains unresolved between two competing models. In the first model the Tharsis Rise is dynamically supported by a thermal plume in the mantle [Kiefer and Hager, LPI Tech. Rep. 89-04 (1989) 48–50; Harder and Christensen, Nature 380 (1996) 507–509; Breuer et al., J. Geophys. Res. 101 (1996) 7531–7542], while the second model attributes the Tharsis anomalies to volcanic construction and its associated lithospheric flexural effects [Turcotte et al., J. Geophys. Res. 86 (1981) 3951–3959; Phillips et al., Science 291 (2001) 2587–2591]. Here we resolve this ambiguity by modeling the ratio of gravity and topography at long wavelengths with a new loading formulation that simultaneously considers plume buoyancy and surface loads. We demonstrate that a thermal plume contributes no more than 15% to the geoid and 25% to the topography for the Tharsis Rise for the range of lithospheric thicknesses that are constrained by observations. This indicates that the Tharsis Rise is best explained by volcanic construction on lithosphere.

Keywords: Mars; Tharsis Rise; gravity and topography anomalies; loading models

1. Introduction

The Tharsis Rise and the crustal dichotomy (i.e., the gradual pole-to-pole topographic variations) are the two most prominent topographic features on Mars (Fig. 1a–c). The crustal dichotomy may have formed in the Early Noachian, while the bulk of the Tharsis Rise may have formed by the Late Noachian [7,8]. Upon removing the first-degree spherical harmonic component of topography (i.e., $l = 1$) associated with the crustal dichotomy, the long-wavelength topography and geoid anomalies are dominated by the Tharsis Rise (Fig. 1b,c and Table 1) [2]. In fact, the Tharsis anomalies can be reproduced well with only degrees 2 and 3 components (Fig. 1d,e). Because of its large size and of its successive tectonic activities and volcanisms that span Noachian to Amazonian times [9], the Tharsis Rise has long been considered the key to understanding the thermal evolution of Mars [10].

While both the plume and volcanic construction models appear to reproduce the elevated to-

* Corresponding author. Tel.: +1-303-735-5095; Fax: +1-303-492-7935.
E-mail address: szhong@spice.colorado.edu (S. Zhong).

0012-821X/03/$ – see front matter © 2003 Elsevier B.V. All rights reserved.
doi:10.1016/S0012-821X(03)00384-4

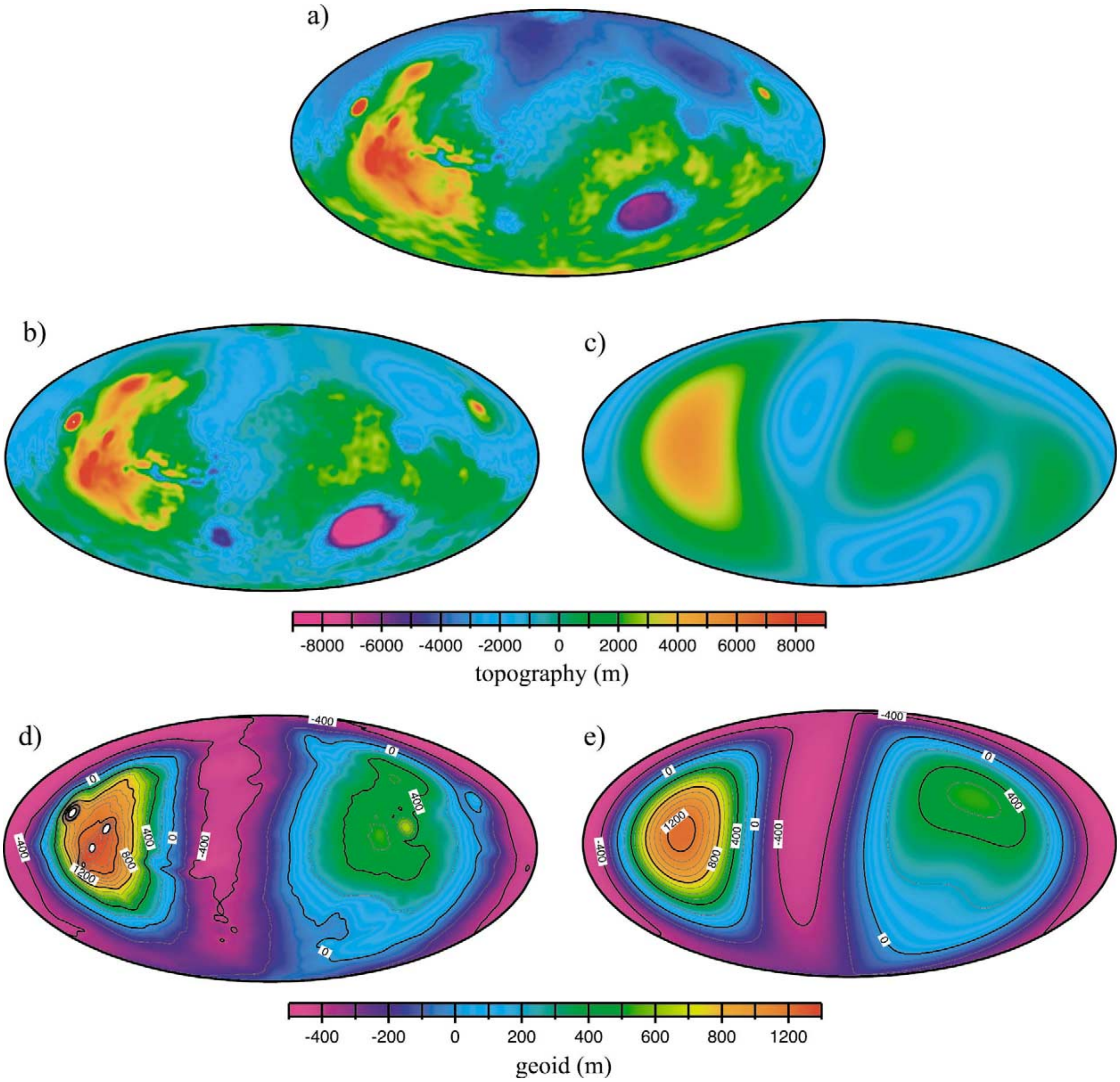

Fig. 1. Martian surface topography and geoid anomalies [1,2]. Topography from degrees 1 to 70 (a), from degrees 2 to 70 (b), and from degrees 2 and 3 (c), and the geoid anomalies from degrees 2 to 70 (d) and from degrees 2 to 3 (e). For the gravity, the J_2 term is reduced by 95% to account for hydrostatic flattening effects.

pography and surface tectonics in the Tharsis region [3,4,6,7], they have different implications for the Martian mantle and crustal structure and for the thermal evolution of Mars. For example, if the Tharsis Rise is supported by a mantle plume, this suggests that the core may be actively cooling, which has implications for the nature of the dynamo and history of the Martian magnetic field. In addition, the plume model would imply no significant crustal thickening in the Tharsis region, as the plume would elevate the crust–mantle interface (i.e., Moho) in a similar way as it does to the surface. This is in sharp contrast with the prediction of a thickened crust and depressed Moho from the volcanic construction model [7,11]. Therefore, it is crucial to distinguish between these two models.

Recently, Zhong [12] found that the geoid anomalies induced by a thermal plume may be significantly reduced by an elastic lithosphere that has been neglected in the previous plume models for the Tharsis Rise (e.g., [4,13]). This reduction in the geoid may reach a factor of 3 at very long wavelengths including $l=2$ for the elastic thickness of 150 km [12] which is consistent with that inferred from modeling topography and gravity of young volcanoes (e.g., Olympus Mons) in the Tharsis region [14]. However, Zhong [12] only considered plume buoyancy loading and did not attempt to use the topography and geoid observations to constrain the origin of the Tharsis anomalies. In this study, by considering plume buoyancy and surface loading simultaneously with a new loading formulation, we assess the relative importance of surface loading processes (i.e., volcanic construction and its associated lithospheric flexural effect) and plume buoyancy to the Tharsis topography and geoid anomalies, thus constraining the origin of the Tharsis anomalies.

2. Models

We consider surface loads and plume buoyancy at some given depth as the two possible sources of loads to which the Tharsis topography and geoid anomalies can be attributed. By modeling the ratio of geoid to topography, $R_{G/T}$, with a new modeling formulation that takes into account simultaneously surface loads and plume buoyancy, and by comparing with the observed $R_{G/T}$, we seek to constrain the relative importance of surface loads and plume buoyancy to the Tharsis anomalies. The observed $R_{G/T}$ is 0.30 and 0.19 at $l=2$ and 3, respectively (Table 1). Here we only consider the long wavelengths at $l=2$ and 3 for two reasons: (1) the Tharsis geoid and topography anomalies are well reproduced by these two harmonics (Fig. 1b–e), and (2) at these two harmonics, the geoid and topography show good correlation (Fig. 1b–e and Table 1). The correlation between topography and geoid at degree 4 is significantly reduced (Table 1), possibly because of the influence of the impact basins (e.g., Hellas basin) that show almost no geoid signal. We think that at wavelengths shorter than those for degrees 2 and 3 other features such as impact basins and volcanoes may influence the Tharsis geoid and topography anomalies significantly.

Table 1
Long-wavelength topography and geoid anomalies

Degree (l)	$R_{G/T}$	Topography[a] (m)	Geoid (m)	Correlation
2	0.30	4275	1283	0.96
3	0.19	3481	655	0.63
4	0.11	1984	223	0.25
5	0.05	2661	123	0.71

[a] RMS power of spherical harmonic expansion of topography and geoid. The spherical harmonic functions are normalized to 1. $R_{G/T}$ is the ratio of the RMS powers of the geoid to topography.

2.1. Model parameters

Our analyses are done in a spherical harmonic domain with a thin elastic shell model [6] for surface loading and a hybrid loading formulation [12] for plume buoyancy loading. There are three controlling parameters in our model: elastic thickness during the formation of the Tharsis rise, T_{e_o}, present-day elastic thickness, T_{e_n}, and depth of plume buoyancy, D_p. Plume buoyancy loading is a dynamic process that is sensitive to present-day elastic thickness T_{e_n}, while surface loading during the formation of the Tharsis rise is controlled by elastic thickness in the Late Noachian T_{e_o} [7]. While T_{e_n} and D_p control the topography and geoid responses to plume buoyancy, T_{e_o} determines the responses to the formation of the Tharsis rise. While these three parameters are treated as variables in our model, they are also constrained by the observations and theoretical studies.

Recent analyses of intermediate- and short-wavelength topography and gravity anomalies of Mars by McGovern et al. [14] suggested that elastic thickness generally increases with time with some rapid increase in the Noachian period and that the elastic thickness for Olympus Mons, a good indicator of T_{e_n}, is $\sim$150 km or greater. This is consistent with other gravity and topography analyses [11] and with predictions of thermal evolution modeling of Mars [15–17]. A smaller elastic thickness for Olympus Mons was also suggested based on admittance analyses of gravity and topography [18]. However, McGovern et al. [14] suggested that the analyses in [18] did not adequately filter out contributions from other tectonic features that have smaller elastic thickness than that for Olympus Mons, thus underestimating the elastic thickness for Olympus Mons. Modeling tectonic features including tilted valley networks [7] and strain fields [19] that are believed to be associated with the formation of the Tharsis Rise suggests that T_{e_o} is $\sim$100 km. In our study, we assume that $T_{e_o} = T_{e_n}/\alpha$ where α is >1 and possibly $\sim$1.5, but we treat both T_{e_n} and α as variables.

While plume buoyancy may be distributed at all depths [4], plume buoyancy that is capable of producing the elevated topography at wavelengths comparable with the size of the Tharsis (i.e., $l=2$ and 3) only occurs at relatively shallow depths below the lithosphere where plume material spreads out [12]. In this study, we consider only these long-wavelength components of plume buoyancy. A constraint on the depth of long-wavelength plume buoyancy D_p is the depth of melting for plume material, because the depth of melting is generally larger than the depth of plume material that spreads out beneath the lithosphere [20]. A thermal evolution modeling suggests that the depth of melting for thermal plumes beneath the Tharsis region is currently $\sim$250 km [18]. Considering the uncertainties in this estimate [18], we think that a reasonable upper bound on D_p is 450 km.

D_p can also be related to T_{e_n} and the thickness of the top thermal boundary layer. This is because T_{e_n} is defined by lithospheric thermal structure (e.g., $\sim$550°C for Earth's oceanic lithosphere [21–23]) that also controls the depth to which the plume can ascend before it spreads out horizontally. We recast D_p as $D_p = \beta T_{e_n}$, where β is a multiplier. While β varies from 2 to 4 in our models, we think that β should be $\sim$3. For thermal convection with a strongly temperature-dependent rheology, the top thermal boundary layer consists of a stable upper layer and unstable sub-layer [24]. This sub-layer with $\sim$200 K temperature difference [24] is subject to thermo-mechanical erosion by thermal plumes [20]. This implies that the top of the plume may reach to a depth of $\sim 2T_{e_n}$, for mantle potential temperature $\sim$1300°C. The thickness of the plume material that spreads out beneath the lithosphere should be comparable to that for the top thermal boundary layer. Therefore, the central depth of the horizontally spreading plume D_p should be $\sim 3T_{e_n}$. This is fully consistent with numerical modeling of plume dynamics for the Hawaiian swell on Earth [20,25]. Elastic thickness for the Hawaiian swell is suggested to be 44 km after the effects of the seamount are corrected for [22], while numerical modeling of plume dynamics in [20,25] shows that the horizontally spreading plume below the Hawaiian swell is located at a depth of $\sim$110 km.

2.2. Modeling procedures

Our modeling approach consists of the following three steps for each harmonic degree. (1) The ratio of geoid to topography for surface loading, R_{G/T_S}, is computed for different elastic thicknesses using the thin elastic shell formulation [6] to get $R_{G/T_S} = R_{G/T_S}(T_{e_o})$ (notice that $T_{e_o} = T_{e_n}/\alpha$). (2) The ratio of geoid to topography for plume buoyancy loading, R_{G/T_I}, is computed for different T_{e_n} and β to get $R_{G/T_I} = R_{G/T_I}(T_{e_n},\beta)$, using a hybrid loading formulation in [12]. (3) Using $R_{G/T_S} = R_{G/T_S}(T_{e_o})$ and $R_{G/T_I} = R_{G/T_I}(T_{e_n},\beta)$ from steps 1 and 2, we solve for all the possible solutions of T_{e_n}, α, and β that can produce the observed $R_{G/T}$. These different solutions may lead to different relative contributions from surface loading and plume buoyancy loading to the surface observations. We determine the fractions of observed geoid and topography that are attributable to plume buoyancy for these solutions.

Now we explain each of these three modeling steps. The thin elastic shell formulation (see Table 2 for model parameters) in [6] for surface loading has been widely used in modeling planetary topography and gravity anomalies (e.g., [7,14,18]).

Table 2
Model parameters

Parameter	Value
Planetary radius	3400 km
Gravitational acceleration	3.73 m/s^2
Poisson's ratio	0.25
Young's modulus[a]	1.4×10^{11} Pa
Crustal thickness	50 km
Crust density	2900 kg/m^3
Mantle density	3400 kg/m^3
Core radius	1700 km

[a] Young's modulus is taken from [18]. Crustal thickness and density are taken from [11].

The thin shell model is fully applicable at long wavelengths considered here [26]. The response to internal loads for a viscous mantle underlying an elastic shell (i.e., used in our step 2) is computed by using the radial stress on the surface predicted from a purely viscous flow model [5,13,27] as the loads to the same thin elastic shell model used in step 1. The inclusion of the thin elastic shell model is the only difference between this hybrid approach [12] and that in [5,13,27]. The hybrid approach was found to reproduce well the surface topography predicted from a more complete viscoelastic formulation [12].

The radial stress on the surface from the purely viscous flow model depends only on relative variation in mantle viscosity [27]. We employ a simple mantle viscosity structure that includes a weak layer where the plume buoyancy is located to simulate the temperature dependence of viscosity. The thickness of the weak layer is $2T_{e_n}$ and its viscosity is 20 times smaller than that of the underlying mantle. However, our tests show that the results are insensitive to the viscosity structure, because the plume buoyancy is at relatively shallow depths [27]. Also because of the shallow loading depths, the contribution of core–mantle boundary deformation to the geoid is also negligibly small, although its effects are included in our calculations. Just as in the thin elastic shell model for surface loading, the upward displacement of the Moho due to the plume buoyancy and its contribution to the geoid are also included.

If we define f_t as the fraction of observed topography due to the plume buoyancy (i.e., $f_t = H_{pl}/H_{obs}$, where H_{obs} is the observed uplift and H_{pl} is the elevated topography produced by a plume), then $1-f_t$ is the fraction of observed topography due to surface loads. For plume buoyancy at a depth of βT_{e_n} with an elastic shell of thickness T_{e_n}, and surface loads on an elastic shell with thickness T_{e_o}, the following equation holds:

$$(1-f_t)R_{G/T_S}(T_{e_o}) + f_t R_{G/T_I}(T_{e_n}, \beta) = R_{G/T} \quad (1)$$

where $R_{G/T}$ is the observed ratio of geoid to topography, and $R_{G/T_S}(T_{e_o})$ and $R_{G/T_I}(T_{e_n},\beta)$ are from steps 1 and 2. To solve Eq. 1 for f_t as a function of T_{e_n}, α, and β, we employ the following iterative scheme.

For given f_t, α and β, (1) Give an initial guess for T_{e_n}. (2) For the given T_{e_n}, evaluate R_{G/T_I} from the relation $R_{G/T_I} = R_{G/T_I}(T_{e_n},\beta)$. (3) For R_{G/T_I} from the preceding step, solve for R_{G/T_S} from $R_{G/T_S} = (R_{G/T} - f_t R_{G/T_I})/(1-f_t)$ which is derived from Eq. 1. (4) From the resulting R_{G/T_S}, invert for T_{e_o} from the relation $R_{G/T_S} = R_{G/T_S}(T_{e_o})$. (5) Evaluate $\varepsilon = |\alpha T_{e_o} - T_{e_n}|/T_{e_n}$. If $\varepsilon < 1\%$, a solution for T_{e_n} is found. Otherwise, let $T_{e_n} = \alpha T_{e_o}$ and return to step 2 of the iteration. We also terminate the iteration if a convergent solution cannot be found for T_{e_n} that is between 50 km and 250 km.

This iterative scheme determines all the possible solutions of T_{e_n}, α, and β that produce the observed $R_{G/T}$ and the corresponding f_t. However, we consider only the following parameter ranges: 50 km $\leq T_{e_n} \leq$ 250 km, $1.25 \leq \alpha \leq 2$, and $2 \leq \beta \leq 4$. Once f_t is determined, the fraction of observed geoid due to plume buoyancy f_g can be obtained with:

$$f_g = f_t \frac{R_{G/T_I}(T_{e_n}, \beta)}{R_{G/T}} \quad (2)$$

3. Results

We now present model predictions of the ratio of geoid to topography for surface loading, R_{G/T_S}, and for plume buoyancy loading, R_{G/T_I}, and their dependence on elastic thickness and other parameters. At spherical harmonic degrees 2 and 3, R_{G/T_S} increases with T_e (Fig. 2) [6,12] and R_{G/T_S} are the same as observed for $T_e \approx$ 90–100 km.

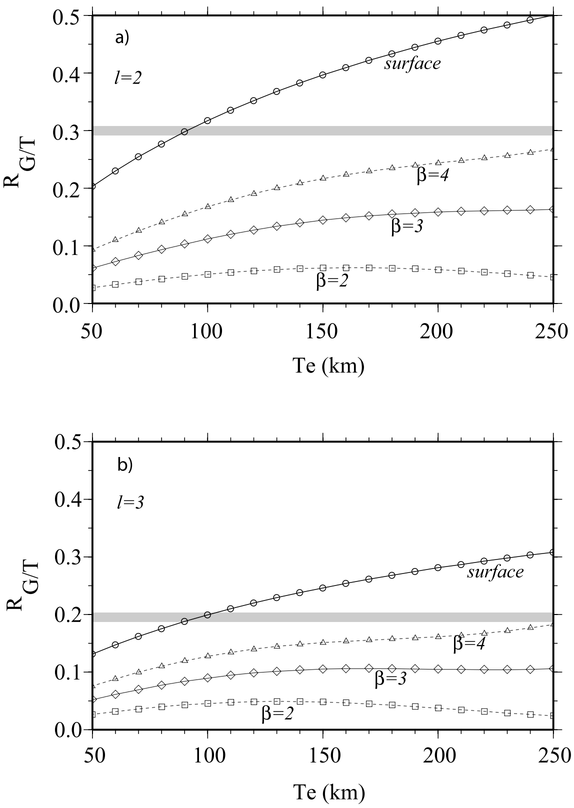

Fig. 2. Ratios of geoid to topography for surface loading with different elastic thicknesses (the line with open circles) and for plume buoyancy loading with different elastic thicknesses and different loading depths (i.e., different β) for degrees 2 (a) and 3 (b). Because the calculations for surface loading are independent of those for plume buoyancy loading, we do not distinguish T_{e_o} from T_{e_n} here. The shaded bars in a and b indicate the observed values.

This implies that if we attribute all the observed geoid and topography anomalies to surface loading processes associated with the formation of the Tharsis rise in the Late Noachian [7], then T_e needs to be $\sim$90–100 km, which is consistent with previous studies [7,19].

The ratio of geoid to topography for plume buoyancy loading, R_{G/T_I}, depends on both T_e and loading depth (i.e., β). For a fixed T_e, R_{G/T_I} increases with β (Fig. 2) and thus also loading depth [12]. For a fixed β, R_{G/T_I} generally increases with T_e, but for $\beta<2$, R_{G/T_I} may decrease with T_e for large T_e (Fig. 2), indicating the filtering effects of an elastic shell on internal loads [12]. These results suggest that for $\beta<4$, plume buoyancy loading alone cannot explain the observed $R_{G/T}$ even for $T_e \approx 250$ km and $D_p \approx 1000$ km (Fig. 2). Notice that we do not distinguish between T_{e_n} and T_{e_o} in Fig. 2, and this is because these calculations for R_{G/T_I} and R_{G/T_S} are independent of each other.

Although surface loading with $\sim$90–100 km thick elastic shell explains the observed $R_{G/T}$ at long wavelengths, other solutions are also possible if plume buoyancy loading is allowed. Now let us examine these possible solutions in terms of T_{e_n}, α, and β. For $\alpha=1.5$ (i.e., $T_{e_n}=1.5T_{e_o}$), observed $R_{G/T}$ at degrees 2 and 3 can be explained for $T_{e_n}>136$ km, but depending on loading depths or β, f_g and f_t may vary significantly (Fig. 3a–d). f_g and f_t are 0 for $T_{e_n} \approx 136$ km (or $T_{e_o} \approx 90$ km with $\alpha=1.5$). This is simply the surface loading scenario that we discussed earlier. For a fixed T_{e_n}, f_g and f_t increase with β (i.e., larger loading depth). For example, at degree 2, for $T_{e_n}=150$ km as suggested in [14] from studying the loading of the Olympus Mons, f_g is 0.02, 0.05, and 0.13, for $\beta=2$, 3, and 4 (or $D_p=300$ km, 450 km, and 600 km), respectively (Fig. 3a). The results are similar at degree 3. f_t is larger than f_g (e.g., Fig. 3a,c), as expected from Eq. 2 with R_{G/T_I} that is smaller than the observed $R_{G/T}$ (Fig. 2).

Our results are moderately sensitive to α, the ratio of T_{e_n} to T_{e_o}. For given T_{e_n} and loading depth or β, a larger α tends to decrease f_g (Fig. 3e,f). For a given β, a larger α would also require a larger T_{e_n} in order to achieve the same f_g. For example, for $\beta=3$, to achieve $f_g=0$, minimum T_{e_n} values of 160 km and 181 km are required for $\alpha=1.75$ and 2.0, respectively (Fig. 3e,f). McGovern et al. [14] suggested that T_{e_n} up to 200 km is also possible. $T_{e_n} \approx 200$ km corresponds to $\alpha \approx 2$. For $\alpha=2$, $T_{e_n}=200$ km, and $\beta=3$ (or $D_p=600$ km), f_g is $\sim$0.06 (Fig. 3g,h). However, it is unclear whether the plume melting can occur in this case with the large plume buoyancy depth D_p.

Our results indicate that the plume buoyancy may not contribute more than 15% of the observed geoid. If we require $D_p<450$ km, with $\alpha=1.5$, f_g reaches a maximum of 5% when $\beta=3$ and $T_{e_n}=150$ km (Fig. 3a,b). Notice from our earlier discussions, $T_{e_n} \approx 150$ km, $\beta \approx 3$, and

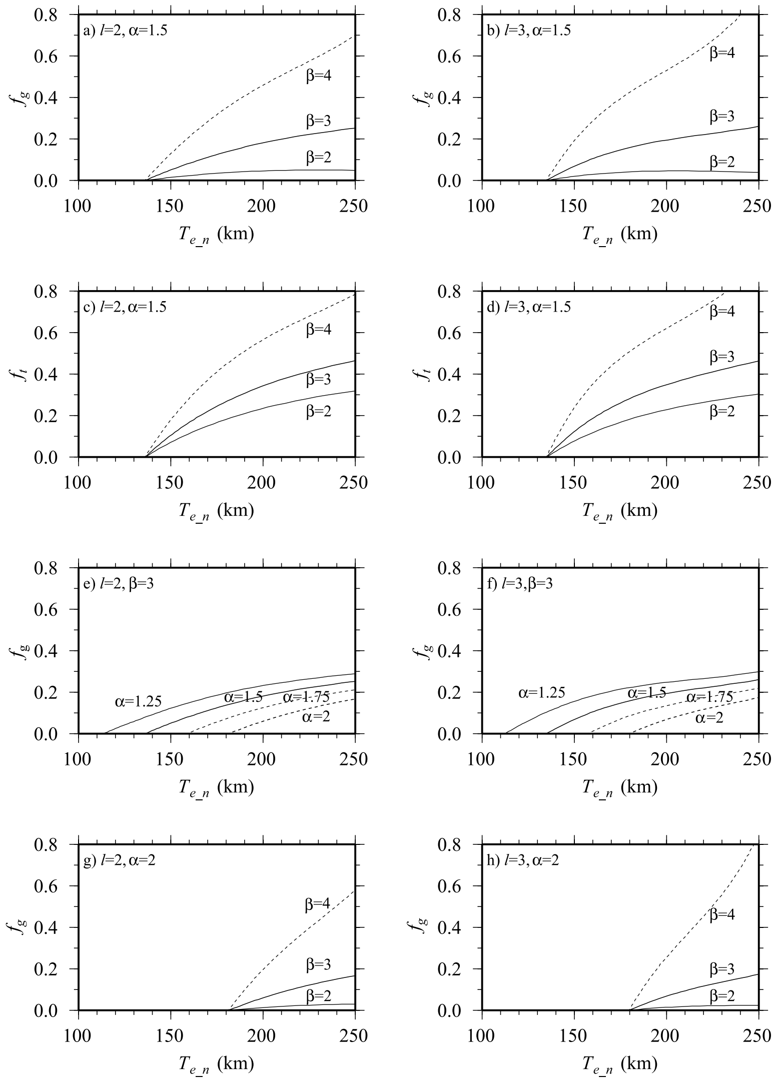

Fig. 3. The dependence of the fraction of the observed geoid due to plume buoyancy f_g on T_{e_n} and loading depth βT_{e_n} for $T_{e_o} = T_{e_n}/\alpha$ where $\alpha = 1.5$ and spherical harmonic degrees $l = 2$ (a) and $l = 3$ (b), the dependence of the fraction of the observed topography due to plume buoyancy f_t on T_{e_n} and loading depth βT_{e_n} for $T_{e_o} = T_{e_n}/1.5$ and $l = 2$ (c) and $l = 3$ (d), the dependence of f_g on T_{e_n} and T_{e_o} for $\beta = 3$ and $l = 2$ (e) and $l = 3$ (f), and the dependence of f_g on T_{e_n} and loading depth βT_{e_n} for $\alpha = 2$ and $l = 2$ (g) and $l = 3$ (h).

$\alpha \approx 1.5$ are our preferred parameters. For $\alpha = 1.25$, the maximum f_g of $\sim 12\%$ occurs when $\beta = 3$ and $T_{e_n} = 150$ km (Fig. 3e,f), but $T_{e_o} = 120$ km. For $\alpha = 1.75$ or 2, f_g is even smaller. For $T_{e_o} \approx 100$ km [7,19], if we require $T_{e_n} \approx 150$ km and 200 km [14], for f_g to reach 20%, D_p needs to be greater than 600 km and 800 km, respectively (Fig. 3a,b,g,h), which may be too deep to produce melting in the plume. Considering the possible range for T_{e_n} (150–200 km), β (2.5–3.5) and α (1.5–2), we think that $f_g < 15\%$. With the same requirements, we estimate that $f_t < 25\%$. Our results also suggest that elastic thickness should be at least 90 km when the Tharsis Rise was formed (Figs. 2 and 3).

Our estimates of plume buoyancy contributions are insensitive to crustal thickness. For example, to increase our 50-km crustal thickness [11] (Table 1) by 50% influences our estimate of maximum f_g by no more than 3%. To reduce Young's modulus from 1.4×10^{11} Pa to 10^{11} Pa, for $T_{e_n}=200$ km, $\beta=3$, and $\alpha=1.5$, f_g remains less than 0.07.

4. Discussion and conclusions

The very long-wavelength (i.e., degrees 2 and 3) geoid and topography anomalies on Mars are dominated by the Tharsis Rise (Fig. 1). By modeling the ratio of geoid to topography at these wavelengths from surface loads and plume buoyancy loads, we demonstrate that the plume buoyancy may not contribute more than 15% of the observed geoid and 25% of the observed topography for the Tharsis Rise, provided that present-day elastic thickness is ~150–200 km [14], elastic thickness during the formation of the Tharsis Rise in the late Noachian is ~100 km [7,14], and long-wavelength components of plume buoyancy are located at depths shallower than 600 km. The long-wavelength plume buoyancy at degrees 2 and 3 that is relevant to the Tharsis Rise only occurs at relatively shallow depths where plume material spreads out laterally below the lithosphere. Our modeling indicates that this plume buoyancy alone cannot produce the observed ratio of geoid to topography (i.e., 0.2–0.3) for a reasonable range of parameters of plume loading depth and elastic plate thickness (Fig. 2).

A mantle plume may not be effective in producing geoid anomalies, although it may cause significant uplift at the surface. For example, the Hawaiian swell with ~1 km topography that is most likely related to a mantle plume only displays a few meters geoid anomalies with the ratio of geoid to topography of ~0.005 [28]. In their original plume models for the Tharsis Rise, Harder and Christensen [4] showed that while a one-plume structure reproduced the elevation of the Tharsis Rise, the plume explained only ~10% of the Tharsis geoid anomalies. Later, Harder [13] was able to get larger geoid anomalies by including a thicker viscous lithosphere that pushes plume buoyancy to a larger depth to result in a larger ratio of geoid to topography [12]. However, the elastic effects of lithosphere were excluded in [4,13], and they can greatly reduce the geoid from a plume, especially for relatively thick lithosphere [12].

Our results suggest that a dynamic support for the elevated Tharsis topography and geoid anomalies from a plume is untenable and that the anomalies are best explained by the volcanic construction on the lithosphere. However, this also raises a question as to how such a large volcanic/igneous province like the Tharsis Rise was formed. On Earth, formations of a large volume of flood basalts have been attributed to the melting associated with a rising plume head [29]. The Tharsis Rise may have been produced with a similar dynamic process associated with a rising plume head, possibly with one-plume thermal structure [4]. The remaining, though diminished, plume [30] may still provide the heat source for young volcanoes such as Olympus Mons in the Tharsis region.

Acknowledgements

We thank Patrick McGovern, Roger Phillips, Norm Sleep, Tilman Spohn, and Donald Turcotte for their helpful reviews and Maria Zuber for commenting on the manuscript. This research is supported by NASA Grant NAG5-11224, the David and Lucile Packard Foundation and the Alfred P. Sloan Foundation.***[SK]***

References

[1] D.E. Smith et al., The gravity field of Mars: Results from Mars Global Surveyor, Science 286 (1999) 94–97.
[2] D.E. Smith et al., The global topography of Mars and implications for surface evolution, Science 284 (1999) 1495–1503.
[3] W.S. Kiefer, B.H. Hager, The role of mantle convection in the origin of the Tharsis and Elysium provinces of Mars (abstract), in: Early Tectonic and Volcanic Evolution of Mars, LPI Tech. Report 89-04 (1989) 48–50.
[4] H. Harder, U. Christensen, A one-plume model of Martian mantle convection, Nature 380 (1996) 507–509.
[5] D. Breuer, H. Zhou, D.A. Yuen, T. Spohn, Phase transitions in the Martian mantle: Implications for the plan-

et's volcanic evolution, J. Geophys. Res. 101 (1996) 7531–7542.
[6] D.L. Turcotte, R.J. Willemann, W.F. Haxby, J. Norberry, Role of membrane stresses in the support of planetary topography, J. Geophys. Res. 86 (1981) 3951–3959.
[7] R.J. Phillips et al., Ancient geodynamics and global-scale hydrology on Mars, Science 291 (2001) 2587–2591.
[8] R.C. Anderson et al., Primary centers and secondary concentrations of tectonic activity through time in the western hemisphere of Mars, J. Geophys. Res. 106 (2001) 20563–20585.
[9] K.L. Tanaka, Scott, D.H., Greeley, R., Global stratigraphy, in: H.H. Kieffer et al. (Eds.), Mars, University of Arizona Press, Tucson, AZ, 1992, pp. 345–382.
[10] S.C. Solomon, J.W. Head, Heterogeneities in the thickness of the elastic thickness of Mars: Constraints on heat flow and internal dynamics, J. Geophys. Res. 95 (1990) 11073–11083.
[11] M.T. Zuber et al., Internal structure and early thermal evolution of Mars from Mars Global Surveyor topography and gravity, Science 287 (2000) 1788–1793.
[12] S. Zhong, Effects of lithosphere on the long-wavelength gravity anomalies and their implications for the formation of the Tharsis rise on Mars, J. Geophys. Res. 107 (2002) 10.1029/2001JE001589.
[13] H. Harder, Mantle convection and the dynamic geoid of Mars, Geophys. Res. Lett. 27 (2000) 301–304.
[14] P.J. McGovern et al., Localized gravity/topography admittance and correlation spectra on Mars: Implications for regional and global evolution, J. Geophys. Res. 107 (2002) 10.1029/2002JE001854.
[15] G. Schubert, T. Spohn, Thermal history of Mars and the sulfur content of its core, J. Geophys. Res. 95 (1990) 14095–14104.
[16] D.J. Stevenson, T. Spohn, G. Schubert, Magnetism and thermal evolution of terrestrial planets, Icarus 54 (1983) 466–489.
[17] S.A. Hauck II, R.J. Phillips, Thermal and crustal evolution of Mars, J. Geophys. Res. 107 (2002) 10.1029/2001JE001801.
[18] D. McKenzie, D.N. Barnett, D.H. Yuan, The relationship between Martian gravity and topography, Earth Planet. Sci. Lett. 195 (2002) 1–16.
[19] W.B. Banerdt, M.P. Golombek, K.L. Tanaka, Stress and tectonics on Mars, in: H.H. Kieffer et al. (Eds.), Mars, University of Arizona Press, Tucson, AZ, 1992, pp. 249–297.
[20] N.M. Ribe, U.R. Christensen, The dynamical origin of Hawaiian volcanism, Earth Planet. Sci. Lett. 171 (1999) 517–531.
[21] M.K. McNutt, Lithospheric flexure and thermal anomalies, J. Geophys. Res. 89 (1984) 11180–11194.
[22] P. Wessel, A reexamination of the flexural deformation beneath the Hawaiian islands, J. Geophys. Res. 98 (1993) 12177–12190.
[23] A.B. Watts, J.H. Bodine, N.M. Ribe, Observations of the flexure and geological evolution of the Pacific Ocean basins, Nature 283 (1980) 532–537.
[24] S.V. Solomatov, L.N. Moresi, Scaling of time-dependent stagnant convection: Application to small-scale convection on Earth and other terrestrial planets, J. Geophys. Res. 105 (2000) 21795–21817.
[25] S. Zhong, A.B. Watts, Constraints on the dynamics of mantle plumes from uplift of the Hawaiian islands, Earth Planet. Sci. Lett. 203 (2002) 105–116.
[26] S. Zhong, M.T. Zuber, Long-wavelength topographic relaxation for self-gravitating planets and its implications to the compensation of lunar basins, J. Geophys. Res. 105 (2000) 4153–4164.
[27] B.H. Hager, M.A. Richards, Long-wavelength variations in Earth's geoid: Physical models and dynamical implications, Phil. Trans. R. Soc. London Ser. A 328 (1989) 309–327.
[28] K. Marks, D.T. Sandwell, Analysis of geoid height versus topography for oceanic plateaus and swells using nonbiased linear regression, J. Geophys. Res. 96 (1991) 8045–8055.
[29] W.J. Morgan, Hotspot tracks and the opening of the Atlantic and Indian oceans, in: C. Emiliani (Ed.), The Sea, vol. 7, Wiley Interscience, New York, 1981, pp. 443–475.
[30] T. Spohn, M.H. Acuna, D. Breuer, M. Golombek, R. Greeley, A. Halliday, E. Hauber, R. Jaumann, F. Sohl, Geophysical constraints on the evolution of Mars, Space Sci. Rev. 96 (2001) 231–262.